Journal of Applied Geophysics 200 (2022) 104614

Contents lists available at ScienceDirect

Journal of Applied Geophysics

journal homepage: www.elsevier.com/locate/jappgeo

Cuspate-lobate folding in glacial sediments revealed by a small-scale 3-D seismic survey

Hermann Buness [a,*], David Colin Tanner [a], Thomas Burschil [a,1], Gerald Gabriel [a,c], Ulrike Wielandt-Schuster [b]

[a] Leibniz Institute for Applied Geophysics, Stilleweg 2, 30655 Hannover, Germany
[b] Regierungspräsidium Freiburg, Landesamt für Geologie, Rohstoffe und Bergbau (LGRB), Albertstraße 5, Freiburg im Breisgau D-79104, Germany
[c] Institute of Geology, Leibniz University Hannover, Calllinstraße 30, 30167 Hannover, Germany

ARTICLE INFO

Keywords:
Cuspate-lobate folding
Glacial sediments
CRS-processing
3-D seismic data
Electrodynamic seismic vibrator

ABSTRACT

We carried out a small-scale 3-D seismic survey (120 × 120 m^2, bin size 1.5 m) in advance of a research borehole. The target consists of 150 m of Quaternary sediments in a glacially overdeepened valley. We used a wheelbarrow-mounted electrodynamic vibrator as seismic source and chose a simple orthogonal layout. During one week of acquisition, we fired 1024 shots into 384 vertical geophones.

The key processing step was the interpolation and regularization of traces, realized by common reflection surface (CRS) processing. This enhances data quality in low fold regions at small offsets. Despite the small source, the entire Quaternary fill and the base of the valley is imaged well.

At a depth of 20–50 m, glaciotectonic deformation, in the form of cuspate-lobate folds, is visible, which was not recognized previously in a 2-D seismic profile that runs along the edge of the 3-D area. The folding indicates that compressional glacial stresses acted on layers of stiff till and less competent clastics. We interpret that the varying fold axes' directions indicate varying stress fields during the Last Glacial Maximum. Cuspate-lobate folding has hitherto not been used to describe the deformation of glacial sediments.

1. Introduction

Glacial and post-glacial sediments are found in many regions of the world where Quaternary glaciation has left its footprint. They are often very heterogeneous due to the dynamic behaviour of glaciers; thus their characterization using boreholes and imaging by geophysics is challenging. Although glacial sediments were extensively eroded in post-glacial periods, they are often conserved in overdeepened glacial valleys (Huuse and Lykke-Andersen, 2000; Buechi et al., 2017). These valleys trap sediment that contain information about the past climate conditions. An ambitious program to reveal the climate history of the Alpine glaciations was started in 2021 (Anselmetti et al., 2016), in the framework of the International Continental Drilling Program (ICDP). This project will probe all major catchment areas of the Alps using boreholes. One of these drill sites is the Tannwald Basin, an overdeepened valley excavated by the Rhine Glacier during the Hoßkirchian ice age (Ellwanger et al., 2011), about 50 km north of Lake Constance (Fig. 1).

Burschil et al. (2018) used a network of high-resolution 2-D seismic profiles to reveal the shape and the infill of the 250 m-deep Tannwald Basin, which led to the proposed location of the drill site (Fig. 1). To clarify the detailed tectonic situation before drilling, we carried out two small-scale (~120 x ~ 120 m^2) 3-D seismic surveys, one conducted with two orientations of a horizontal source and 3-component receivers (Burschil et al., 2020), the other one with a vertical source and receivers. This paper focuses on the latter.

3-D surveys are not common in the near-surface,[2] because of the increased effort that is necessary to image shallow reflectors with respect to deeper ones, within the same area. The maximal minimum offset is linearly related to the depth of the shallowest, to-be fully imaged

* Corresponding author.
E-mail addresses: Hermann.Buness@leibniz-liag.de (H. Buness), DavidColin.Tanner@leibniz-liag.de (D.C. Tanner), Thomas.Burschil@leibniz-liag.de (T. Burschil), Gerald.Gabriel@leibniz-liag.de (G. Gabriel), Ulrike.Wielandt-Schuster@rpf.bwl.de (U. Wielandt-Schuster).
[1] Current affiliation: Federal Institute for Geosciences and Natural Resources, Stilleweg 2, 30655 Hannover, Germany.
[2] Since 'near-surface' is not a well-defined term, we define it here to indicate depths from 20 to 200 m, whereas even shallower seismic surveys often are termed ultra-shallow (Bachrach and Nur, 1998; Schmelzbach et al., 2007; Sloan et al., 2009)

https://doi.org/10.1016/j.jappgeo.2022.104614
Received 17 December 2021; Received in revised form 15 March 2022; Accepted 16 March 2022
Available online 20 March 2022

reflector (Cordsen et al., 2000). Hence, the total length of shot- and receiver lines of orthogonal layouts increases quadratically. Moreover, near-surface reflections are often richer in high frequencies than deeper reflections. To avoid wavefield aliasing, both geophone- and shot-spacing have to be reduced.

Near-surface 3-D seismic studies, in the sense of our definition, have been carried out for many tasks, e.g., fault recognition (Schmelzbach et al., 2007; Kaiser et al., 2011), geohazards (Sargent and Goulty, 2009; Lundberg et al., 2016), environmental issues (House et al., 1996), and hydrology (Mari and Porel, 2007). ETH Zurich pioneered near-surface 3-D measurements in the Suhre Valley in a comparable glacial environment (Büker et al., 1998, 2000). They set up a primary orthogonal layout with shot/receiver distances of 3–9/3 m and line distances of 6/12 m. Because for most of the common midpoints (CMP) only 1–2 traces fell in the offset range up to 20 m, they decided to set up a secondary near-offset source-receiver pattern. This secondary pattern was responsible for about half of the entire field effort (Spitzer et al., 2001): for an area of 320 × 420 m^2 a crew of six needed 85 days, accomplishing more than 12,000 shots. In order to reduce this effort, Spitzer et al. (1998, 1999) simulated a doubling of shot and receiver distances and used the flex-binning technique (Brune et al., 1994; Lu et al., 1996) to maintain the same bin size as the original survey. This technique fills empty bins with traces of neighbouring CMP, but leaves others unchanged. They conclude that a reduction of the field effort up to 75% still yields a comparable image quality to the original survey. However, flex-binning should only be used in regions that are underlain by low- or moderately-dipping structures (Spitzer et al., 1998).

In this study, we conducted a much simpler 3-D survey in terms of acquisition effort. To overcome the problems that result from the irregular offset distribution of the orthogonal layout, we used a common reflection surface (CRS)-processing scheme (Hubral et al., 1998; Jaeger et al., 2001; Hertweck et al., 2007) to regularize the pre-stack gathers. Furthermore, we used a lightweight, electrodynamic, wheelbarrow-mounted source ('ELVIS', Polom et al., 2011), with a peak force of about 1 kN that performed well in previous testing (Burschil et al., 2021).

1.1. Geological setting

The Tannwald Basin is a north-south elongated, about 1 km wide and up to 250 m deep overdeepened basin. It was excavated by the Rhine Glacier during the Hoßkirchian stage, mainly into Tertiary Upper Freshwater Molasse. In its deepest part, it even reaches in to the Upper Marine Molasse (Ellwanger et al., 2011). Its sedimentary infill was analysed by a research borehole, drilled in 1993 (borehole 'Schneidermartin', Fig. 1b), and a network of five, newly-acquired, P-wave seismic reflection profiles (Fig. 1b); described in Burschil et al., 2018).

The infill of the basin comprises sediments from three glacial phases (Fig. 2). After initial glacial erosion during the Hoßkirchian (D3 discontinuity), sedimentation began with a waterlain till (A). This is represented in the seismic sections by strong reflectors. At the same time, the glacier plucked slabs of molasse blocks from the valley floor, and deposited them in the deepest part of the basin (M'). Above this, less reflective, basinal, fine-grained sediments were deposited with a thickness of more than 100 m (B). In their lower part (B-2), they consist of marly and silty, fining-upward beds, in the upper part upwards-coarsening foresets (B-1). The fines were deposited from Hoßkirchian to early Rißian, as part of the Dietmanns basin sediments (Ellwanger et al., 2011). Coarse-grained clastics and intercalated till layers of the Scholterhaus Formation (early Rißian) follow above the basin sediments (C-1). After a discontinuity, they are followed by an up to 5 m thick till sequence (C-2) of Rißian age (Illmensee Formation, Ellwanger et al., 2011). Finally, the sequence is capped by about 10 m of glaciofluvial gravels (E) of the outwash (sandur, Wurmian, Fig. 1b), that formed peripheral to the terminal moraine of the Last Glacial Maximum (LGM). This push moraine is about 200 m away to the SW of the drill site (Fig. 1b).

1.2. Survey

The aim of the 3-D seismic survey was characterization of the sedimentary sequence and structure in the proximity of the planned research borehole. We deemed an area of 100 × 100 m^2 to be sufficient for this task and determined the following parameters (Fig. 3), with the help of a

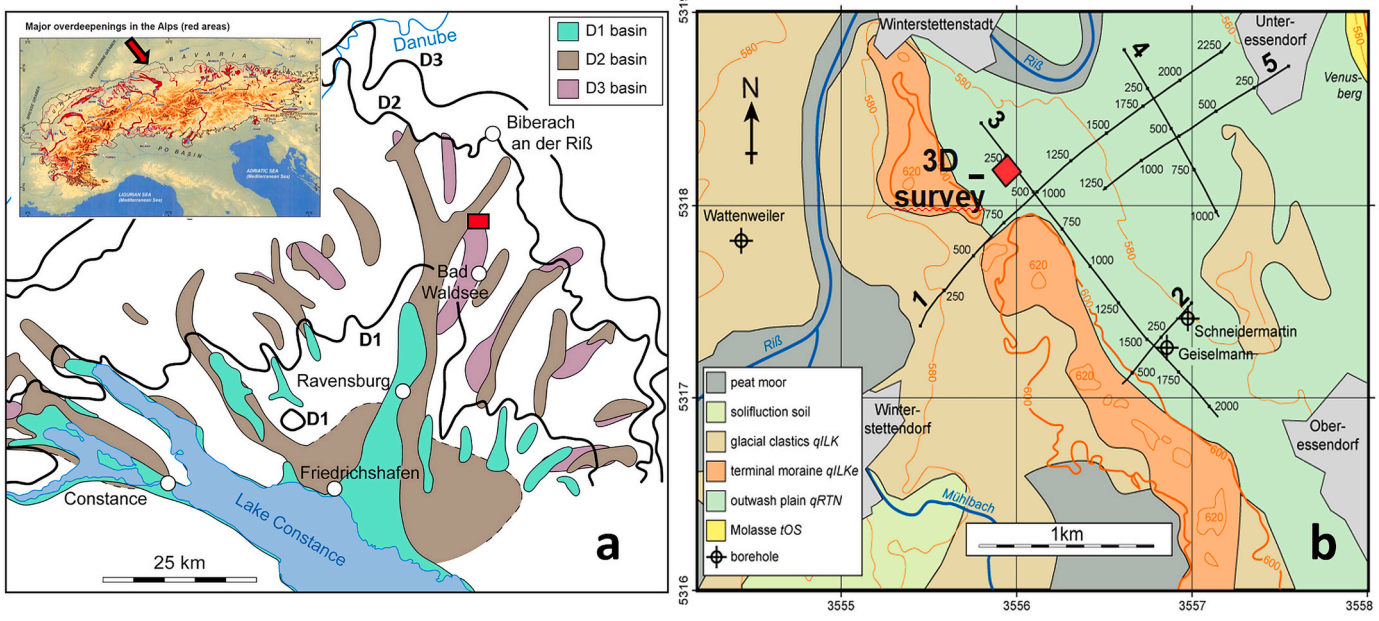

Fig. 1. (a) System of basins carved by the Rhine glacier north of Lake Constance. D3 – D1 are major regional unconformities developed in Hoßkirchian, Rißian and Würmian glacial stages, respectively. The red arrow and the red box mark the investigation area. (b) geological map of the survey site with boreholes, 2-D seismic profiles (black lines, 1–5) and the 3D seismic survey (red box) covering the proposed drilling site. Note the proximity of the LGM terminal moraine to the survey area. (For interpretation of the references to colour in this figure legend, the reader is referred to the web version of this article.)

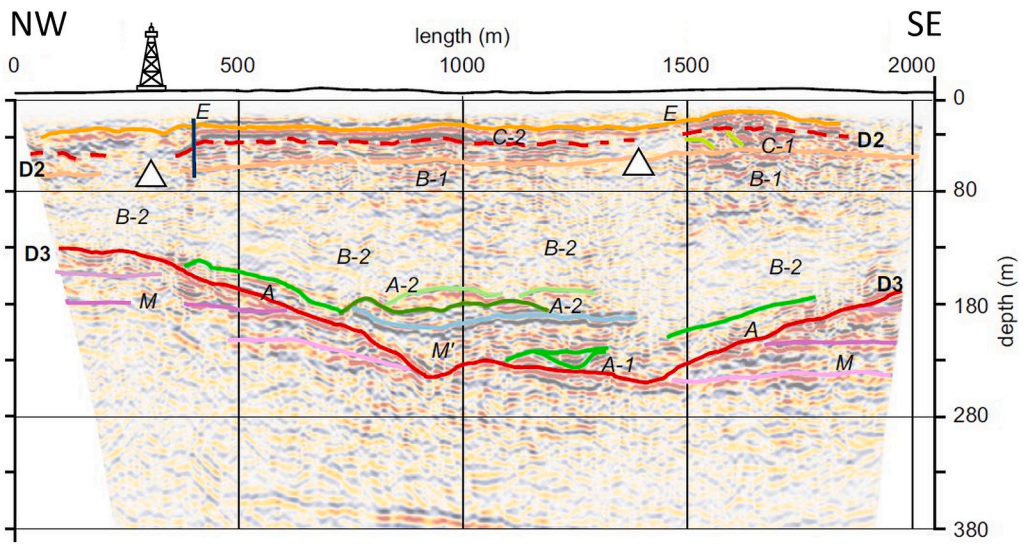

Fig. 2. P-wave seismic Section 3 and interpretation, taken from Burschil et al. (2018): M - Upper Freshwater Molasse (tOS), M' - allochthonous molasse slab, lodgement till, A-1 - trough structure, A-2 - esker, B - basinal fine-grained deposits (Dietmanns basin sediment), B-1, B-2, C - till sequences and till, C-1 - Scholterhaus Sfm., C-2 - Duermentingen Sfm, E - fluvial deposits, sand/gravel, outwash plains, D3 and D2 - regional unconformities separating major deposition/ erosion cycles occurring in mid-Hoßkirchian and mid-Rißian glacial periods. The drill rig indicates the proposed well location. White triangles mark regions with poor imaging quality.

2-D seismic profile that runs alongside the site (cf. Fig. 2):

- Bin size: The maximum size to avoid aliasing can be formulated as:

$$binsize < \frac{V_{min}}{4\, f_{max}\, sin\alpha}$$

where V_{min} is the minimum velocity, f_{max} is the maximum frequency, and α is the reflector inclination, after Sheriff and Geldart (1995). This formula yields a bin size of 2.5 m, using $V_{min} = 1000$ m s^{-1}, $f_{max} = 200$ Hz, and $\alpha = 30°$. Since we want to compare this survey to an S-wave survey carried out previously at the same location, we adopted the bin size of 1.5 m, which is rather conservative for this survey, giving a geophone spacing of 3 m.

- Line spacing: This defines the fold and the mapping of shallow reflectors. As a rule of thumb, the maximal minimum offset should be 1.0–1.2 times the depth of the shallowest reflector (Cordsen et al., 2000). Taking into account the number of available channels and the size of the area we wanted to cover, a line spacing of 9 m was realized without the need for more than one patch. This geometrically limits shallow imaging to depths greater than 10 m. In favour of symmetrical sampling (Vermeer, 2004), we kept the same values for the shot lines that run orthogonal to the receiver lines.
- Shots: The area covered by shots has to exceed the area covered by geophones to ensure a sufficient minimal maximum offset. Imaging of the base of the basin at 150 m depth requires an offset of about 100 m, with regards to the 'optimum window technique' (Hunter et al., 1984). This requires shot points to be extended about 50 m outside the area covered by receiver lines. To limit the field effort, we doubled the shot distance to 6 m outside the receiver lines (Fig. 3).

The recording equipment consisted of 16 seismographs with 24 channels and 384 vertical geophones (Table 1). We used the electrodynamic source – ELVIS (Polom et al., 2011), a wheelbarrow-mounted device that has very little impact on the environment. This was required to obtain permission to enter arable land and to avoid field damage (Fig. 4). A 10 s sweep of 20–200 Hz was excited twice at each of the 1004 realized shot positions. The whole survey was completed within 5 days of field operation with a crew of 3–4. Geodetic measurements took an additional half-day.

1.3. Processing

The raw data are dominated by refracted, guided, and surface waves, with no reflections visible (Figs. 5a,b and 6a,b). The wide azimuth acquisition resulted in a strong scatter of the reflection and refraction onsets in the shot gather, as well as in the CMP gather (Fig. 6a,b). The scatter could be reduced partly by refraction static; ~380.000 first arrivals were picked using a neural net, and, where necessary, corrected manually.

At first, we applied a number of pre-stack processing steps (1–7 in Table 2), i.e., vertical stack of shots at the same position, refraction static, bottom mute to eliminate air blast and surface waves, spectral whitening considering the sweep frequencies, followed by a time variable bandpass to enhance high frequencies, especially at small travel times, and automatic gain control. A 3-D f-k filter applied to these data still did not yield clear reflections (Figs. 6d, 7b).

In order to enhance the signal/noise ratio, we applied the common reflection surface (CRS) technique. The CRS method takes dip, azimuth and curvature of a local reflector element into account and defines a spatial stacking operator that extends both in midpoint and offset directions, whereas the well-known normal moveout (NMO) formula only considers offset. Dips and azimuths of reflector surfaces are necessary to construct the CRS operator and are determined in a preliminary zero-offset stack. Since the quality of the stack was rather low so far (Fig. 7a,b), we initially calculated the CRS-operator with dip values set to zero and iteratively determined dips and azimuths. The velocity analysis started with NMO velocities and was also iteratively refined. The spatial aperture of the CRS operator determines the number of neighbouring bins that are sampled into one CRS bin. It has a major effect on stack quality – a larger value provides a better signal/noise ratio at the cost of resolution. We found an optimum value of 4–5 m for our interpretation. This is only half the value of the first Fresnel zone in the upper part and much less in deeper parts.

The CRS-regularization achieved better-populated gathers, favouring the application of multi-trace processes (Figs. 6e, 7c). In our case, we used an f-k filter to attenuate refracted, guided, and S-waves (Figs. 6f, 7d). The velocity analysis on regularized and f-k filtered CRS gathers was clearer than on conventionally-built supergathers. We found low stacking velocities near the surface that start with values of only 900 m s^{-1}, considerably lower than previously found on the 2-D seismic profile that cuts the survey area. However, the aliasing criterion for the bin size is still satisfied. The top of the water table was expected at a depth of around 35–40 m. After Kirchhoff prestack-time migration, residual moveout was picked on migrated gathers and applied to the data

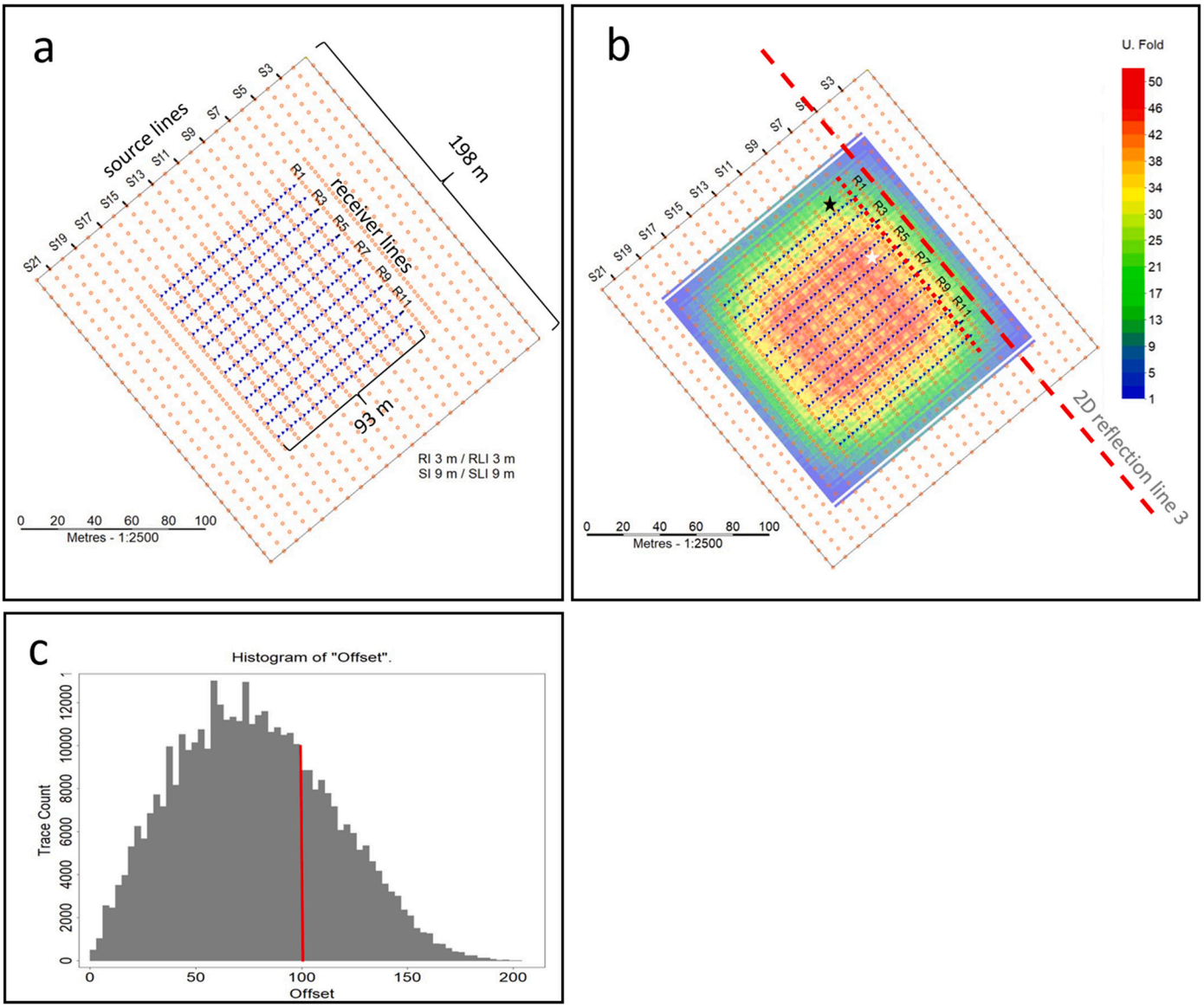

Fig. 3. Layout of 3-D survey (a) source and receiver lines, (b) unique fold using an offset bin size of 3 m, (c) offset distribution of all traces, the red line indicates the required minimal maximum offset of 100 m. The black and the white star in (b) mark the position of shotpoint 340 and CMP 3529 used in Figs. 5 and 6. The dashed red line gives the position of the 2-D line, the dotted red line the position of inline 20 used in Figs. 7 und 8. (For interpretation of the references to colour in this figure legend, the reader is referred to the web version of this article.)

Table 1
Recording parameters.

# source lines / # receiver lines	22 / 12
Point / line spacing	3 m / 9 m
# CMP / CMP bin size	9600 / 1.5 m × 1.5 m
# inlines / # crosslines	100 / 95
area covered by receiver / shots / cmp	93 × 99 m^2/ 189 × 198 m^2 / 148.5 × 141 m^2
Source (peak force)	ELVIS-VII (1kN)
# source points planned / # realized / # excitations	1014 / 1004 / 2
Source signal / duration / frequency range	linear sweep / 10 s / 20–200 Hz
Geophone type, resonance frequency	Sensor SM-6, 20 Hz
# geophones / # receiver positions / # channels	384 / 384 / 384
Seismographs (# seismographs)	Geometrics Geode (16)
Recording, listening time, sampling interval	uncorrelated, 12 s, 2 ms

(Figs. 6g, 7e). Given the small extent of the survey, we used a single velocity function, averaged from the 16 analysis locations, after stack to convert the volume to depth.

1.4. Results and interpretation

After depth conversion and adjustment to the final datum, the volume was compared to the 2-D line (Figs. 8, 9). The inline shown in Fig. 8a is the same as shown in Fig. 7e. It is located 15 m in front of the 2-D line and shares the same overall features: strong reflections from the upper till sequences (cf. Fig. 2) at 10–50 m depth, a transparent section below indicating the basin fines, and the basin base at a depth of ~140–150 m. However, the most distinct difference between the 3-D and 2-D sections is the former's much higher resolution of the upper till sequences and the overlying glaciofluvial sediments of the outwash plain. Whereas in the 2-D section only a blurred pattern can be recognized, a distinct folding pattern appears in the upper till sequences in the 3-D data. This folding is seen as well as on crosslines and random lines

Fig. 4. 3-D seismic survey acquisition, (a, b) the ELVIS source operating in different field conditions, (c) hardly visible traces after source operation.

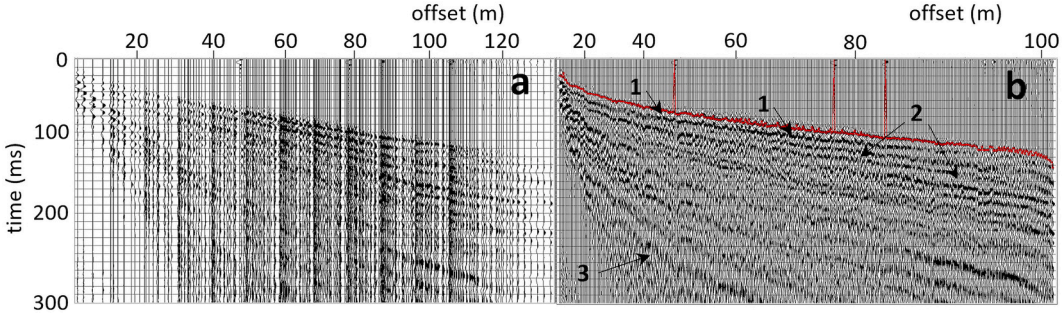

Fig. 5. Shotpoint 340, raw data with (a) variable trace spacing and (b) constant trace spacing. Trace equalization applied for display. First arrivals are indicated by red points. Note the low trace density at small offsets. Position marked in Fig. 3b. (For interpretation of the references to colour in this figure legend, the reader is referred to the web version of this article.)

(Fig. 9).

We interpret the folds of the upper till sequences as cuspate-lobate folding (Ramsay, 1967; Ramsay and Huber, 1987). The cusps point downwards, the lobes close upwards. In 3-D, there are three orientations of fold axes. The youngest fold axes plunge horizontally SE-NW (white lines – N137°, Fig. 10, termed here 'major' axes). There are two other directions of folding visible in Fig. 10 (green – N48° and blue – N77°), which are clearly offset by the major fold axes and thus older.

The wavelength of the folding varies between 40 m and 80 m, and the amplitude of the folds is on average about 20 m. Folding terminates downwards into the basin fines that do not show a pronounced reflectivity; hence, a lower boundary cannot be clearly established. Above the cuspate-lobate folding, reflectivity, as well as the continuity of the reflections, decreases.

We found only one clearly visible thrust fault that cuts through the upper till sequences (Fig. 8b). The fault ends at top of the lower part of the upper till units, the relationship to an arching element of the uppermost reflector at a depth of 10 m is not clear due to the resolution of the seismic image. The fault strikes SE-NW, similar to the major fold axes.

2. Discussion

2.1. Methodology

We used a small, wheelbarrow-mounted electrodynamic source ('Elvis VII', Polom et al., 2011), with a peak force of about 1 kN. This source enabled us access to several land properties, since it left nearly no impact on the environment (cf. Fig. 3c). Thus, it is suitable for application in, e.g. environmental sensitive areas, such as nature reserves and in urban environments. Despite its low peak force, the deepest reflector of interest, the basin base, is imaged in a very comparable quality to the previously shot 2-D seismic profiles (Fig. 8a). These were acquired using a four tonne hydraulic vibrator (MHV4P, c.f. Burschil et al., 2018) that reaches a peak force of 30 kN.

Tests made in advance to the 3-D survey with ELVIS VII revealed that even the deepest part of the basin base, at more than 200 m depth, could be imaged (Burschil et al., 2021). Frequencies recorded in raw data show a drop of more than 20 db along the sweep range. Several steps in the processing influenced the spectral content; in the end, we found a usable frequency content of up to 180 Hz (Fig. 6) that contributed to the stack. Using the Rayleigh criterion for vertical seismic resolution (Sheriff and Geldart, 1995), a value of 1.25 m was achieved in the final depth-converted sections (Figs. 8 and 9).

The sharing of traces between adjacent CMP to enable subsequent regularization is the key step in improving the image quality in this survey, since the simple orthogonal layout causes an irregular offset distribution with a lack of small offsets in shot point as well as in CMP domain. The advantage of CMP processing for low-fold areas is well known (e.g. Eisenberg-Klein et al., 2008; Baykulov and Gajewski, 2009; Gierse et al., 2009). The number of summed CMP can be defined by the spatial aperture of the operator, which in our case gave an optimal image with a value of 4–5 m. This is about 22 times the area of a single bin. The CRS processing thus increases the fold: Inline 20 (cf Fig. 7, 8a) originally has a fold of 56 at its centre that decreases rapidly to the edges. The CRS stack enhances this fold up to 400. The 2-D seismic profile with shot/receiver distances of 5.0/2.5 m reaches a near uniform fold of 96.

In last decade, another technique has emerged that promises to tackle sparse sampling at near offsets, such as in our simple orthogonal layout; 5-D regularization (Trad, 2009; Poole and Wombell, 2010; Jin, 2010). This technique uses five dimensions, i.e. inline, xline, time, offset, and azimuth for a simultaneous interpolation of a 3-D dataset, which exploits the fact that the dimensions are connected by the wavefield and possess differing bandwidths along these dimensions. Application has shown that the technique enhances image quality, particularly within the shallow overburden (Otto, 2017).

2.2. Tectonic development

The most prominent feature in the 3-D seismic volume is the cuspate-lobate folding of the upper till sequence. We interpret the strong and

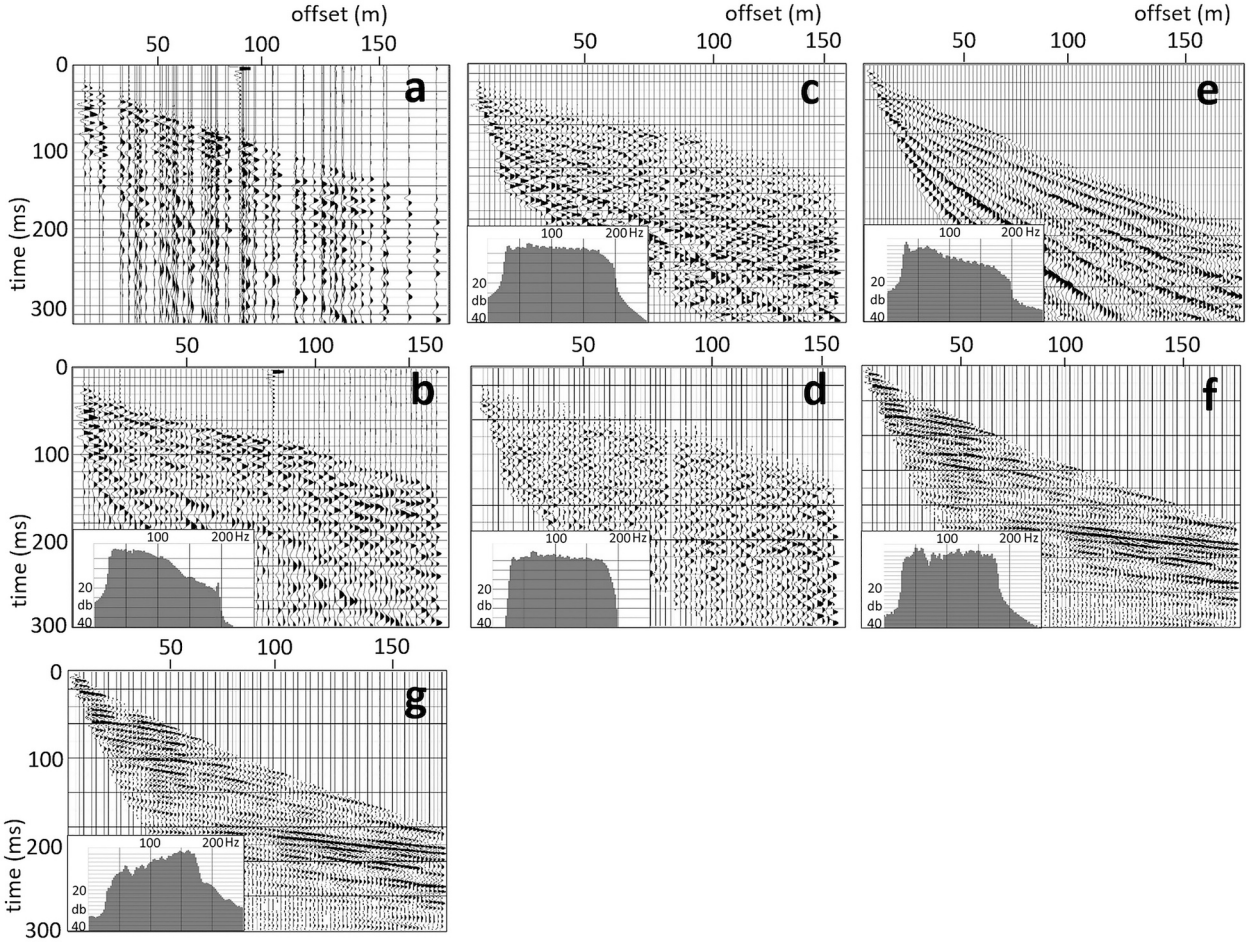

Fig. 6. Application of processing steps, exemplified by CMP 2539; (a) raw data, variable trace spacing, (b) raw data, constant trace spacing, (c) data after standard prestack processing, (d) with additional 3-D f-k filter, (e) data after CRS regularization, (f) with additional 2-D f-k filter, (g) with additional prestack time migration and residual moveout correction.

Table 2
Main processing steps.

1	vertical stack (two shots at each position)	9	CRS binning and regularization (aperture 4–5 m)
2	first break picking using a neural network	10	f-k filter (high pass velocity > 1600 m s^{-1})
3	refraction static (diminishing residual matrix)	11	velocity analysis (iterative)
4	bottom mute (air blast and surface waves)	12	Kirchhoff pre-stack time migration
5	spectral whitening 25/30–180/240 Hz	13	residual moveout correction
6	time variable bandpass (<100 ms: 60–180 Hz, >100 ms: 40–180 Hz)	14	CRS stack
7	automatic gain control, window length 300 ms	15	time-to-depth conversion (final datum 600 m)
8	CRS dip search in preliminary stack (iterative)		

continuous reflectors, at a depth of 20 to 50 m, as multiple till layers intercalated with fluvial clastics, which were deposited at the base of the Ilmensee Formation (i.e. Rißian, Ellwanger et al., 2011). Because cuspate-lobate folding implies a viscosity contrast (>4) between two layers, with the lobes within the more viscous material (Ramsay and Huber, 1987), we infer the upper till layer to be more mechanically competent, at least with respect to the outwash plain clastic sediments above.

Based on the findings of Burschil et al. (2018) and the sedimentary log of the Schneidermartin borehole, all the folded units belong to the Rißian, i.e. the till and overlying outwash plain sediments, and they are topped by unfolded (outwash) sediments of the Würmian. We thus conclude deformation most probably occurred during the LGM in this area, i.e. Würmian. The survey site is situated just 200 m NE of the geologically-mapped terminal moraine, of same age (Figs. 1, 10, 11; Ellwanger et al., 2011). According to these authors, this moraine wall, which is the most conspicuous in the Alpine Foreland, is a push moraine, where the compression came from the SW. We envisage the terminal moraine was deposited as folding took place; therefore the directions of glacier push, i.e. the local compressive stresses, were similar. This would explain the major SE-NW trending fold axes visible in Figs. 10 and 11. However, previous fold axes with other orientations also occur. These may be explained by other subordinate directions of compression before the major event (Figs. 10, 11). One thrust fault is clearly visible in the seismic volume, optimally imaged on crossline 29 (Figs. 9, 10). This indicates that the strongest compressive stress, which caused failure of the till package, was also oriented NE-SW.

Glacial push-moraine deformation (also known as ice-shove or glacier-snout tectonics) in the form of folding and/or thrusting is very typical, in fact more the rule than the exception, and its appearance has been recognized over one hundred years ago (e.g., Fuller, 1914; Croot, 1987; Hambrey, 1994; Hart et al., 1990; Hart and Bolton, 1991; Boulton et al., 1999; Brandes and Le Heron, 2010). However, often folding is recognized from topographic morphologies or surface outcrops (e.g. Croot, 1987); more rarely using geophysical methods, such as ground-penetrating radar (Goetz et al., 2010) or seismic (Clement et al., 2010;

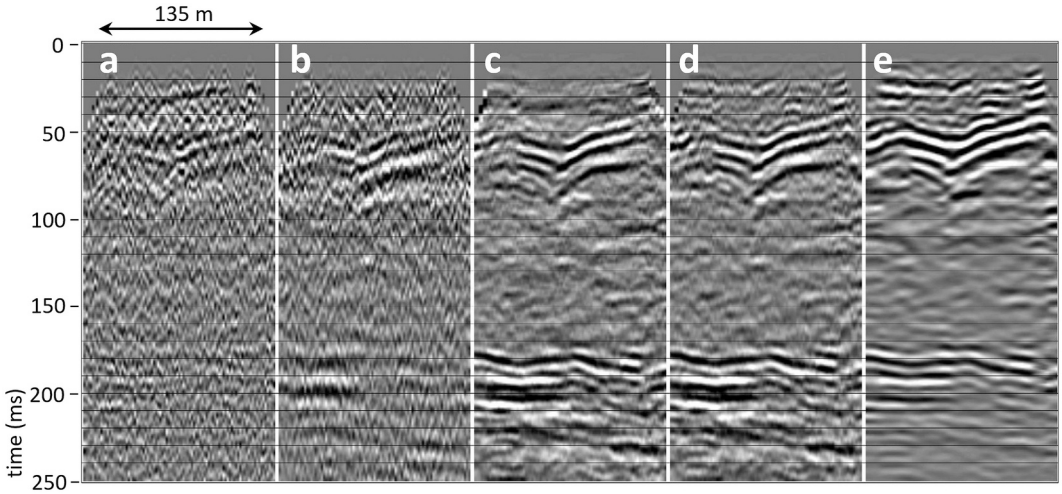

Fig. 7. Application of processing steps, exemplified by stacked inline 20; (a) standard prestack processing (steps 1–7 in Table 2), (b) additional 3-D f-k filter, (c) CRS regularization, (d) additional f-k filter, (e) additional prestack time migration.

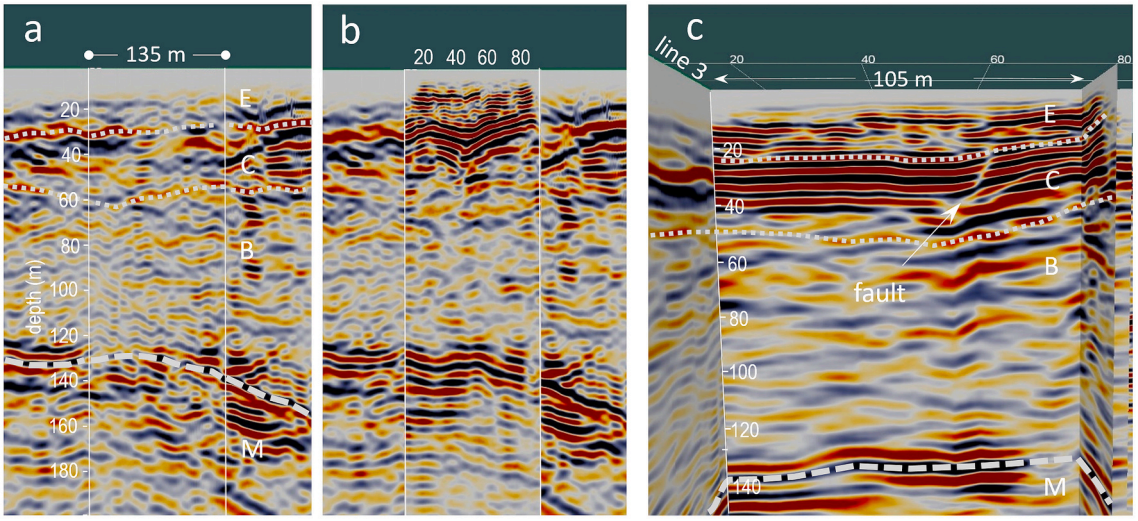

Fig. 8. (a) Original 2-D seismic profile 3 and interpretation, adopted from Burschil et al. (2018). (b) 2-D seismic profile 3 with inline 20 (cf. Fig. 7e) inserted. The inline runs parallel 15 m in front of line 3 and shows cuspate-lobate folding in the upper till sequences. (c) crossline 39 showing a propagating fault (white arrow) in the upper till sequence. Note the better resolution of the 3-D volume compared to the 2-D lines in (a) and (b). Letters E, C, B and M refer to sedimentary units described in Fig. 2. The actual surface is ~10 m above reference datum.

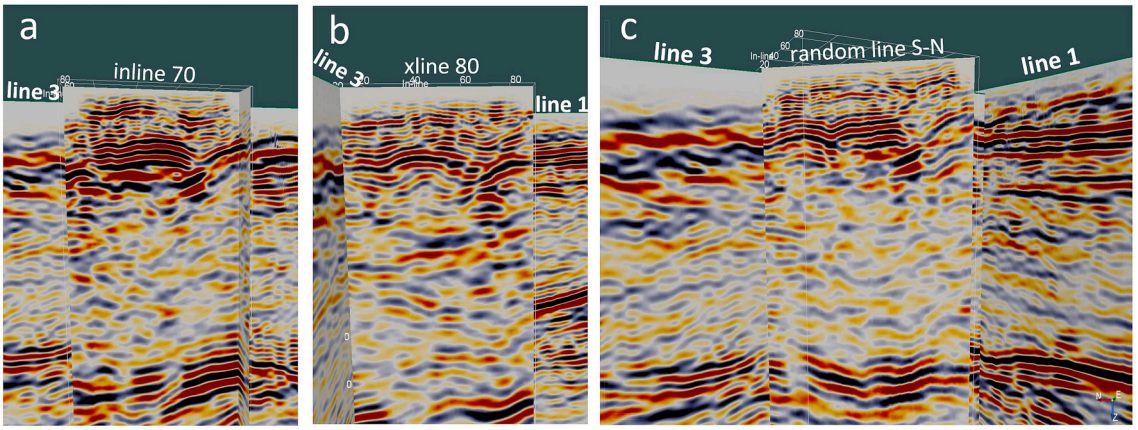

Fig. 9. Cuspate-lobate folding in the upper till sequence on inline 70, crossline 80 and a south-north striking random line. Note the better resolution of the 3-D volume compared to the 2-D lines. The actual surface is ~10 m above reference datum.

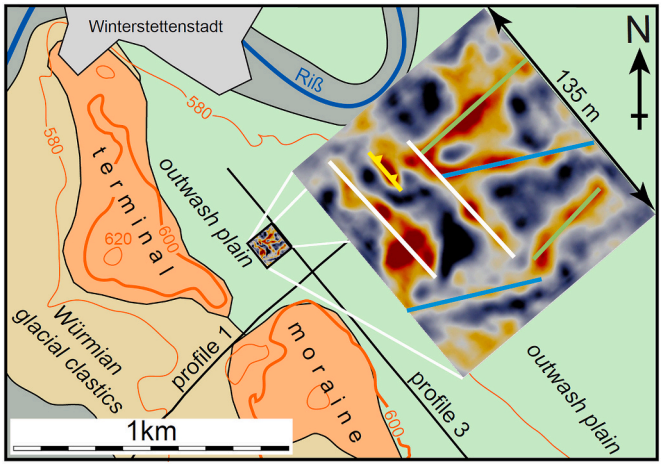

Fig. 10. Simplified geological map of the area, overlain by a depth slice of the 3-D seismic at 29 m depth. Three fold axes'orientations are apparent: green, blue and white, whereby the white major axes are the youngest. The yellow line is the thrust fault strike, ornament on the upthrown side. Seismic profiles 1 and 3 are the 2-D seismic lines referred to in this work. Elevation isolines at every 20 m above sea level. (For interpretation of the references to colour in this figure legend, the reader is referred to the web version of this article.)

Winsemann et al., 2020). Reported folding also ranges in scale from centimetre (e.g., Blignault, 1970) to kilometre scale (e.g., Hayward and Calvert, 2007). Many authors have also attributed the style of deformation to the rheologies of the deformed (glacial) material (e.g. Hart et al., 1990). Nevertheless, in our opinion, no one before has described explicitly cuspate-lobate folding in unconsolidated glacial sediments. For instance, Blignault (1970, p.33) describes: 'Ice-thrust ridges are characteristically sharp crested …. Synclines generally are much wider, their axes being 50 – l00 m apart.' (the more competent layer is therefore above less competent material, as opposed to the case here). This suggests that cuspate-lobate folding *is* commonly observed, but not interpreted as such.

3. Conclusions

Our 3-D survey revealed glacial deformation at shallow depth that was not recognized before on a previous 2-D line running along the survey. The 3-D seismic data undoubtedly show cuspate-lobate folding of upper till and gravel units at a depth of 20–50 m. To our knowledge, this type of folding has never been described before in glaciotectonics. Differing orientations of the fold axes indicate varying maximum horizontal stress directions, but mainly from the SW.

This 3-D survey used a simple orthogonal 3-D layout and was acquired using moderate effort, i.e., a crew of three to four operating for one week. The small electrodynamic vibrator delivered sufficient energy to illuminate the whole 150 m-deep Quaternary sequence and its base.

The low environmental impact of the source would also enable surveys to take place in other sensitive areas, such as on sealed urban surfaces or night operation. Current developments, such as nodal acquisition and more available channels will ease the logistics of 3-D surveys further, since their efficiency depends on channel count. This means 3-D surveys may be more common in the future.

The key step in processing is the regularization of gathers in the pre-stack domain to improve the fold, especially in the low fold, near-offset region. We achieved this by CRS processing, however, other methods, such as 5D regularization, may also work better in the future.

Authors statement

H.B. and T.B. concepted the seismic survey and processed the data.

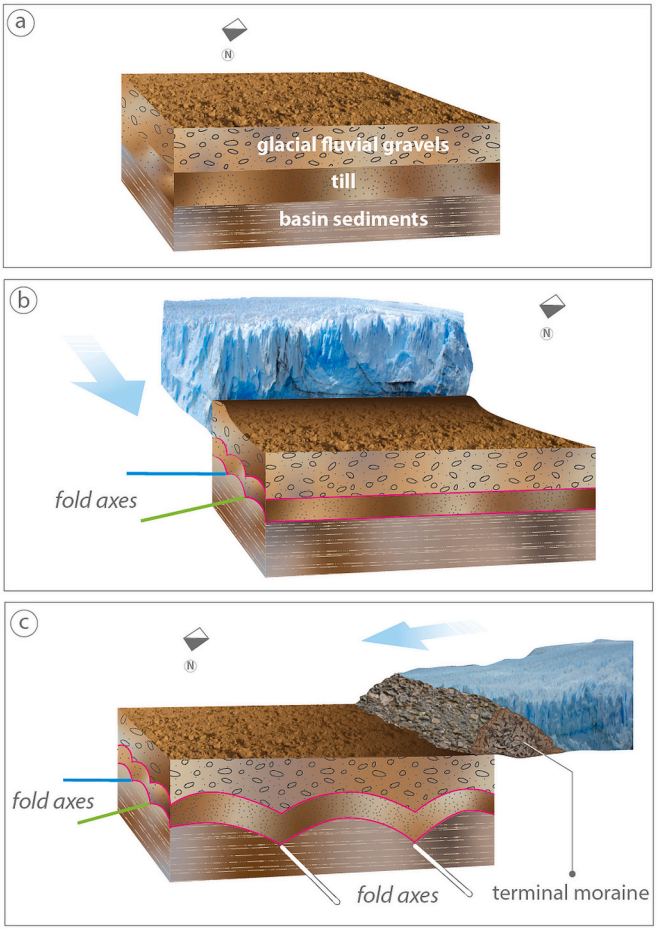

Fig. 11. Schematic development of the envisaged geological development. (a.) Before folding, the till layer is sandwiched between basin fines below and glacial fluvial gravels above. (b.) Ice advance from the south-east produced the first generation of cuspate-lobate folds (blue and green axes, cf. Fig. 10). (c.) Ice advance from the south-west caused the second generation of folds (white fold axes in Fig. 10), as well as the deposition of the terminal moraine. (For interpretation of the references to colour in this figure legend, the reader is referred to the web version of this article.)

D.T. and U.W.-S. interpreted the seismic data. G.G. supervised the project and acquired the funding. All authors contributed to the original draft, editing and revision of the manuscript.

Declaration of Competing Interest

Dr. Hermann Buness reports financial support was provided by German Research Foundation.

Acknowledgments

We thank Frau Hannelore and Herr Johannes Wiedmann for permission to acquire seismic on their land, and our technical staff Jan Bayerle, Jan Bergmann-Baroccas and Erwin Wagner for assistance in the field. Anne-Marie Pogoda-Dorsch drew the cartoon in Fig. 11. We acknowledge funding by the German Research Foundation, grant BU2467/2.

References

Anselmetti, F., Preusser, F., Bavec, M., Crouzet, C., Fiebig, M., Gabriel, G., et al., 2016. Drilling Overdeepened Alpine Valleys (DOVE). ICDP Full Proposal (174 pp).

Bachrach, R., Nur, A., 1998. Same Wavelength GPR and Ultra Shallow Seismic Reflection on a River Point Bar: Sand Stratigraphy and Water Table Complexity: 68th Annual International Meeting, SEG, Expanded Abstracts, pp. 840–843.
Baykulov, M., Gajewski, D., 2009. Prestack seismic data enhancement with partial common-reflection-surface (CRS) stack. Geophysics 74 (3), V49–V58.
Blignault, H.J., 1970. Contemporaneous Glacial Folding in the Table Mountain Group. University of Stellenbosch, Western Cape. M.Sc. thesis. (88pp).
Boulton, G.S., Van der Meer, J.J.M., Beer, D.J., Hart, J.K., Ruegg, G.H.J., 1999. The sedimentary and structural evolution of a recent push moraine complex: Holmstrømsbreen, Spitsbergen. Quat. Sci. Rev. 18, 339–371. https://doi.org/10.1016/S1571-0866(04)80103-9.
Brandes, C., Le Heron, D., 2010. The glaciotectonic deformation of Quaternary sediments by fault-propagation folding. Proc. Geol. Assoc. 121, 270–280. https://doi.org/10.1016/j.pgeola.2010.03.001.
Brune, R.H., O'Sullivan, B., Lu, L., 1994. Comprehensive analysis of marine 3-D bin coverage. Lead. Edge 13, 757–762. https://doi.org/10.1190/1.1437034.
Buechi, M.W., Frank, S.M., Graf, H.R., Menzies, J., Anselmetti, F.S., 2017. Subglacial emplacement of tills and meltwater deposits at the base of overdeepened bedrock troughs. Sedimentology 64, 658–685. https://doi.org/10.1111/sed.12319.
Büker, F., Green, A., Horstmeyer, H., 1998. Shallow 3-D seismic reflection surveying: Data acquisition and preliminary processing strategies. Geophysics 63 (4), 1434–1450. SEG, Tulsa. doi: 10.1190/1.1444444.
Büker, F., Green, A., Horstmeyer, H., 2000. 3-D high-resolution reflection seismic imaging of unconsolidated glacial and glaciolacustrine sediments: Processing and interpretation. Geophysics 65, 18–34. https://doi.org/10.1190/1.1444709.
Burschil, T., Buness, H., Tanner, D.C., Wielandt-Schuster, U., Ellwanger, D., Gabriel, G., 2018. High-resolution reflection seismics reveal the structure and the evolution of the Quaternary glacial Tannwald Basin. Near Surface Geophys. 16 (6), 593–610. https://doi.org/10.1002/nsg.12011.
Burschil, T., Buness, H., Schmelzbach, C., 2020. 3-D Multi-Component S-Wave Survey in the Tannwald Basin: Data Processing and Component Rotation. In: 26th EAGE near surface meeting, online. https://doi.org/10.3997/2214-4609.202020103.
Burschil, T., Buness, H., Leineweber, P., Polom, U., 2021. Results of Performance Tests of Electrodynamic Vibratory Seismic Sources. Ext. abst. 27th EAGE near surface meeting, Bordeaux, France. https://doi.org/10.3997/2214-4609.202120061.
Clement, C.R., Pratt, T.L., Holmes, M.L., Sherrod, B.L., 2010. High-resolution seismic reflection imaging of growth faulting and shallow faults beneath the Southern Puget Lowland, Washington State. Bull. Seismol. Soc. Am. 100 (4), 1710–1723. https://doi.org/10.1785/0120080306.
Cordsen, A., Galbraith, M., Peirce, J., 2000. Planning Land Seismic surveys. Geophysical Developments, no.9, SEG, Tulsa, OK. https://doi.org/10.1190/1.9781560801801.fm.
Croot, D.G., 1987. Glacio-tectonic structures: a mesoscale model of thin-skinned thrust sheets? J. Struct. Geol. 9 (7), 797–808. https://doi.org/10.1016/0191-8141(87)90081-2.
Eisenberg-Klein, G., Pruessmann, J., Gierse, G., Trappe, H., 2008. Noise reduction in 2D and 3D seismic imaging by the CRS method. Lead. Edge 27 (2), 258–265. https://doi.org/10.1190/1.2840375.
Ellwanger, D., Wielandt-Schuster, U., Franz, M., Simon, T., 2011. The Quaternary of the southwest German Alpine Foreland (Bodensee-Oberschwaben, Baden-Wuerttemberg, Southwest Germany). Quaternary Science Journal 60, 306–328. https://doi.org/10.3285/eg.60.2-3.07.
Fuller, M.L., 1914. The Geology of Long Island, New York. U.S. Geol. Survey, Prof. Paper 82.
Gierse, G., Trappe, H., Pruessmann, J., Eisenberger-Klein, G., Lynch, J., 2009. Enhanced velocity analysis, binning, gap infill, and imaging of sparse 2D/3D seismic data by CRS techniques. SEG ext. abs. 2009, 3279-3283, Houston, OK. https://doi.org/10.1190/1.3255541.
Goetz, K.T., Davis, D.M., Cangelosi, M., 2010. Further ground penetrating radar investigations into the Hither Hills glacial tectonism. Long Island Geologists' Abstract Collection, 397. http://hdl.handle.net/11401/64721.
Hambrey, M.J., 1994. Glacial Environments. UBC Press, Vancouver (296 pp).
Hart, J.K., Bolton, G.S., 1991. The interrelation of glaciotectonic and glaciodepositional processes within the glacial environment. Quat. Sci. Rev. 10, 335–350. https://doi.org/10.1016/0277-3791(91)90035-S.
Hart, J.K., Hindmarsh, R.C.A., Boulton, G.S., 1990. Different styles of subglacial glaciotectonic deformation in the context of the Anglian ice sheet. Earth Surf. Process. Landf. 15, 227–241. https://doi.org/10.1002/esp.3290150305.
Hayward, N., Calvert, A.J., 2007. Seismic reflection and tomographic velocity model constraints on the evolution of the Tofino forearc basin, British Columbia. Geophys. J. Int. 168, 643–646. https://doi.org/10.1111/j.1365-246X.2006.03209x.
Hertweck, T., Schleicher, J., Mann, J., 2007. Data stacking beyond CMP. Lead. Edge 26 (7), 818–827. https://doi.org/10.1190/1.2756859.
House, J.R., Boyd, T.M., Haeni, R.E., 1996. A case study for the acquisition, processing, and relevance of 3-D seismic data as applied to the remediation of DNAPL contamination. In: Weimer, P., Davis, T.L. (Eds.), Applications of 3-D Seismic Data to Exploration and Production: Geophysical Developments Series 5: Soc. Expl. Geophys, pp. 257–265. https://doi.org/10.1306/St42605C33.
Hubral, P., Hoecht, G., Jaeger, R., 1998. An introduction to the common reflection surface stack. In: Expanded Abstracts, 60th EAGE meeting, Leipzig, pp. 1–19. https://doi.org/10.1190/1.9781560801917.
Hunter, J.A., Pullan, S.E., Burns, R.A., Gagne, R.M., Good, R.L., 1984. Shallow seismic reflection mapping of the overburden-bedrock interface with the engineering seismograph—some simple techniques. Geophysics 49, 1381–1385. https://doi.org/10.1190/1.1441766.
Huuse, M., Lykke-Andersen, H., 2000. Overdeepened Quaternary valleys in the eastern Danish North Sea: morphology and origin. Quat. Sci. Rev. 19, 1233–1253. https://doi.org/10.1016/S0277-3791(99)00103-1.
Jaeger, R., Mann, J., Hoecht, G., Hubral, P., 2001. Common reflection-surface stack: image and attributes. Geophysics 66 (1), 97–109. https://doi.org/10.1190/1.1444927.
Jin, S., 2010. 5D seismic data regularization by a damped least-norm Fourier inversion. Geophysics 75, Issue 6, Suppl, WB103–WB111. https://doi.org/10.1190/1.3505002.
Kaiser, A., Horstmeyer, H., Green, A., Campbell, F., Langridge, R., McClymont, A., 2011. Detailed images of the shallow Alpine Fault Zone, New Zealand, determined from narrow-azimuth 3D seismic reflection data. Geophysics 76 (1), B19–B32. https://doi.org/10.1190/1.3515920.
Lu, L., Chen, J.J., Bell, L., Lara, R., 1996. 3-D Flex Binning and DMO: 66th Ann. Internat. Mtg., SEG, Expanded Abstracts, pp. 43–46. In: https://onepetro.org/SEGAM/proceedings-pdf/SEG96/All-SEG96/SEG-1996-0043/1957780/seg-1996-0043.pdf.
Lundberg, E., Malehmir, A., Juhlin, C., Bastani, M., Anderson, M., 2016. High-resolution 3D reflection seismic investigation over a quick-clay scar in Southwest Sweden. Geophysics 79 (2), B97–B107. https://doi.org/10.1190/GEO2013-0225.1.
Mari, J.-L., Porel, G., 2007. 3D Seismic Imaging of a Near-Surface Heterogeneous Aquifer: a Case Study. Oil & Gas Science and Technology – Rev. IFP 63, 2, pp. 179–201. https://doi.org/10.2516/ogst:2007077.
Otto, B., 2017. The importance of detailed geological characterization for future expanded use of gas storage in the sustainable energy context. Petroleum Geoscience 23 (3), 327–338. https://doi.org/10.1144/petgeo2016-061. June 27, 2017.
Polom, U., Druivenga, G., Grossmann, E., Grüneberg, S., Rode, W., 2011. Transportabler Scherwellenvibrator. Deutsches Patent und Markenamt. Patentschrift DE10327757B4.
Poole, G., Wombell, R., 2010. Multi-Dimensional Data Reconstruction and Noise Attenuation for Optimal Wide Azimuth Stack. Extended abstract presented at the 72nd EAGE Conference & Exhibition, 14–17 June 2010, Barcelona, Spain. https://doi.org/10.3997/2214-4609.20149949.
Ramsay, J.G., 1967. Folding and Fracturing of Rocks. McGraw-Hill, New York.
Ramsay, J.G., Huber, M.I., 1987. The techniques of modern structural geology. In: Folds and Fractures, vol. 2. Academic Press, London (700 pp.).
Sargent, C., Goulty, N., 2009. Use of 3D seismic to image subsurface foundering due to gypsum dissolution. First Break 27, 61–67. https://doi.org/10.3997/1365-2397.27.1302.32178.
Schmelzbach, C., Horstmeyer, H., Juhlin, C., 2007. Shallow 3D seismic-reflection imaging of fracture zones in crystalline rock. Geophysics 72 (6), B149–B160. https://doi.org/10.1190/1.2787336.
Sheriff, R.E., Geldart, L.P., 1995. Exploration Seismology, 2nd ed. Cambridge University Press, Cambridge. https://doi.org/10.1017/CBO9781139168359. 592 pp.
Sloan, S., Steeples, D., Tsoflias, G., 2009. Ultra-shallow imaging using 3D seismic-reflection methods. Near surface Geophysics 207–314. https://doi.org/10.3997/1873-0604.2009015.
Spitzer, R., van der Veen, M., Nitsche, F.O., Horstmeyer, H., Green, A.G., 1998. Designing 3-D high-resolution seismic surveys. SEG exp. abs. 68 (pp. abstract 234).
Spitzer, R., Nitsche, F.O., Green, A.G., 1999. Reducing field effort in 3-D high-resolution seismic surveying. SEG exp. abs. 69, 512–515. https://doi.org/10.1190/1.1820490.
Spitzer, R., Green, A.G., Nitsche, F.O., 2001. Minimizing field operations in shallow 3-D seismic reflection surveying. Geophysics 66, 1761–1773. https://doi.org/10.1190/1.1487118.
Trad, D., 2009. Five-Dimensional Interpolation: Recovering from Acquisition Constraints, Geophysics, 74, V123. University Press, Cambridge. https://doi.org/10.1190/1.3245216, 592 pp.
Vermeer, G.J.O., 2004. A comparison of two different approaches to 3D seismic survey design. CSEG Recorder 29, 04.
Winsemann, J., Koopmann, H., Tanner, D.C., Lutz, R., Lang, J., Brandes, C., Gaedicke, C., 2020. Seismic interpretation and structural restoration of the Heligoland glaciotectonic thrust-fault complex: Implications for multiple deformation during (pre-)Elsterian to Warthian ice advances into the southern North Sea Basin. Quat. Sci. Rev. 227 https://doi.org/10.1016/j.quascirev.2019.106068, 106088.